

Weak Lensing Study in VOICE Survey II: Shear Bias Calibrations

Dezi Liu^{1,2,3*}, Liping Fu^{2†}, Xiangkun Liu³, Mario Radovich⁴, Chao Wang¹,
Chuzhong Pan¹, Zuhui Fan^{1‡}, Giovanni Covone^{5,6,7}, Mattia Vaccari^{8,9},
Maria Teresa Botticella⁷, Massimo Capaccioli⁵, Demetra De Cicco⁵,
Aniello Grado⁷, Lance Miller¹⁰, Nicola Napolitano⁷, Maurizio Paolillo^{5,6},
Giuliano Pignata^{11,12}

¹Department of Astronomy, School of Physics, Peking University, Beijing 100871, China

²The Shanghai Key Lab for Astrophysics, Shanghai Normal University, 100 Guilin Road, Shanghai 200234, China

³South-Western Institute for Astronomy Research, Yunnan University, Kunming 650500, China

⁴INAF–Osservatorio Astronomico di Padova, vicolo dell’Osservatorio 5, Padova 35122, Italy

⁵Dipartimento di Fisica “E. Pancini”, Università degli Studi Federico II, Napoli 80126, Italy

⁶INFN, Sezione di Napoli, Napoli 80126, Italy

⁷INAF–Osservatorio Astronomico di Capodimonte, Salita Moiariello 16, Napoli 80131, Italy

⁸Department of Physics & Astronomy, University of the Western Cape, Robert Sobukwe Road, 7535 Bellville, Cape Town, South Africa

⁹INAF - Istituto di Radioastronomia, via Gobetti 101, 40129 Bologna, Italy

¹⁰Department of Physics, Oxford University, Keble Road, Oxford OX1 3RH, UK

¹¹Departemento de Ciencias Físicas, Universidad Andres Bello, Avda. Republica 252, Santiago, Chile

¹²Millennium Institute of Astrophysics (MAS), Nuncio Monseñor Sótero Sanz 100, Providencia, Santiago, Chile

Accepted XXX. Received YYY; in original form ZZZ

ABSTRACT

The VST Optical Imaging of the CDFS and ES1 Fields (VOICE) Survey is proposed to obtain deep optical *ugri* imaging of the CDFS and ES1 fields using the VLT Survey Telescope (VST). At present, the observations for the CDFS field have been completed, and comprise in total about 4.9 deg² down to $r_{AB} \sim 26$ mag. Weak lensing shear is measured in a companion paper for *r*-band images with seeing ≤ 0.9 arcsec. In this work, we perform image simulations to calibrate possible biases of the measured shear signals. Statistically, the properties of the simulated point spread function (PSF) and galaxies show good agreement with those of observations. The multiplicative bias is calibrated to reach an accuracy of 3.0%. We study the bias sensitivities to undetected faint galaxies and to the existence of neighboring galaxies. We find that undetected galaxies contribute to 0.3% multiplicative bias. Further analysis shows that galaxies with lower signal-to-noise ratio (SNR) suffer from more significant impact due to the skewed background noise caused by undetected galaxies. Meanwhile, we find that although most of the neighbors have been rejected in the shape measurement procedure, about one third of them still remain in the final shear sample. They show larger ellipticity dispersion and contribute to 0.2% multiplicative bias. Simply rejecting these galaxies can reduce the effective number density of galaxies for deep surveys, such as VOICE. Therefore efficient methods should be developed for future weak lensing surveys in order to decompose their overlapped surface brightness distributions.

Key words: gravitational lensing: weak – methods: data analysis – cosmology: observations

1 INTRODUCTION

The light bundles emitted from distant galaxies are bended when they propagate through the Universe due to the inhomogeneous matter distribution along the line-of-sight. This phenomenon is usually referred as weak gravitational lensing, or cosmic shear (see e.g. Fu & Fan (2014); Kilbinger (2015); Bartelmann & Maturi (2017); Mandelbaum (2017a) for a recent review). The induced galaxy

* E-mail: adzliu@pku.edu.cn

† E-mail: fuliping@shnu.edu.cn

‡ E-mail: fanzuhui@pku.edu.cn

shape distortions reflect directly the gravitational tidal field, and hence contain valuable cosmological information. The observational advances, with the Canada-France-Hawaii Telescope Lensing Survey (CFHTLenS; Heymans et al. (2013)) as a representative one, have made weak lensing effect a powerful cosmological probe (Benjamin et al. 2007; Kilbinger et al. 2013; Heymans et al. 2013; Abbott et al. 2016; Liu et al. 2016). To enhance the power of weak lensing analyses, a number of ongoing and upcoming surveys are motivated to perform accurate measurements of the cosmic shear over larger sky areas, such as the Dark Energy Survey (DES; Becker et al. (2016); Jarvis et al. (2016)), the Hyper Suprime-Cam (HSC) Survey (Miyazaki et al. 2012), the Kilo-Degree Survey (KiDS; Kuijken et al. (2015); Hildebrandt et al. (2017)), the future ground-based Large Synoptic Survey Telescope (LSST; LSST Science Collaboration et al. (2009)), the space-based *Euclid* survey (Laureijs et al. 2011) and the Wide-Field Infrared Survey Telescope (WFIRST; Green et al. (2012)).

It is unfeasible to extract cosmic shear signal from individual galaxy measurement since the intrinsic shape of galaxies is unknown and the shear value is too low to be measured. Therefore, weak lensing studies are statistical in nature, and we need to measure a large number of galaxies. Because the weak lensing induced shape distortion only accounts for a few per cent, much smaller than the intrinsic ellipticity of galaxies, and subjects to many systematics, such as the background noise and intrinsic alignments etc, accurate shear measurement is still challenging. Several programs have devoted many endeavors to test the capabilities of different shear measurement algorithms, and to study their sensitivities to various systematics, such as the imperfect modeling of the variations of the PSF and the telescope observing conditions (Heymans et al. 2006; Massey et al. 2007; Bridle et al. 2009; Kitching et al. 2012; Mandelbaum et al. 2014).

In addition to the instrumental and observational effects (e.g. the spatial and time variations of the PSF, the background noise or observational strategies), the physical properties of galaxies themselves can also bias the shear measurements (Mandelbaum 2017a). For example, the Gravitational Lensing Accuracy Testing 3 (GREAT3; Mandelbaum et al. (2014, 2015)) challenge investigated the impact of the complex galaxy morphology on the measured shear, and concluded that it can affect the calibration by about one per cent for many methods. Hoekstra et al. (2017) also studied the sensitivity of shape measurements to other galaxy properties based on *Euclid*-like image simulation, and highlighted the impact of galaxies below the survey detection limit. Another well known effect is the light contamination from neighboring galaxies. With the increase of survey depth, such blending effect becomes increasingly a concern (Samuroff et al. 2017; Mandelbaum et al. 2017b). As presented in Miller et al. (2013), over 20% of galaxies have neighbors in CFHTLenS, whose i' -band limiting magnitude is $i'_{AB} = 24.54$ mag. These neighboring galaxies are generally excluded for shear measurements because the superposition of their isophotes can lead to large and biased ellipticity estimate. This exclusion does not significantly affect the cosmological studies using CFHTLenS due to their small fraction relative to the total galaxy sample. However, in the case of deeper observations, more galaxies are expected to suffer from blending effect (Chang et al. 2013). For example, 58% of objects in the Hyper Suprime-Cam (HSC) Wide survey are blended (Bosch et al. 2017). Simply excluding these blenders undoubtedly will reduce the effective number density of galaxies considerably and hence degrade the statistical power for cosmological studies. To properly take the blending effect into account to push weak lensing observations to higher redshift, more

robust shape measurement methods and careful systematic calibrations are requested.

In this paper, we perform image simulations based on the VOICE survey (PIs: Giovanni Covone & Mattia Vaccari; Vaccari et al. (2016b)) for shear measurement calibrations. Together with the SUDARE survey (Cappellaro et al. 2015; Botticella et al. 2017), VOICE was proposed to cover about eight square degrees evenly split between the CDFS (Giacconi et al. 2001; Tozzi et al. 2001) and the ES1 (Oliver et al. 2000; Rowan-Robinson et al. 2004) fields in four optical $ugri$ bands using VST/OmegaCam. The survey aims at providing deep optical images in the targeted fields to enable various astrophysical studies in conjunction with other existing data covering different wavelength (Vaccari 2015, 2016a). One of the main scientific objectives is to detect galaxy clusters at intermediate redshifts and determine their two-dimensional mass distributions using the weak lensing shear signals of background galaxies. Started in 2011, the imaging of CDFS field is now completed. Thus we mainly focus on the shear measurements and image simulations in this field. The CDFS field was divided into four tiles (CDFS1–4), each of about one square degree. Over one hundred exposures, spanning almost two years, with a single exposure time of 360 seconds, were obtained for each tile (Falocco et al. 2015). The observation was conducted in dithering mode made of five exposures per epoch which allowed to cover the detector gaps. For each epoch, the exposure times and dithering patterns were the same as in the KiDS survey (de Jong et al. 2015). The images were preprocessed (including flat fielding, cosmic ray removal etc.) with the VST-Tube pipeline (Grado et al. 2012). Selecting only those images with a full width at half maximum (FWHM) less than 0.9 arcsec, the final mosaic reaches a 5σ limiting magnitude of $r_{AB} \sim 26.1$ mag with $2''$ aperture diameter for point source, 1.2 mag deeper than KiDS. The galaxy shape measurements are performed using LensFit (Miller et al. 2007; Kitching et al. 2008; Miller et al. 2013) on the r -band images (Fu et al. 2018, in preparation; F18 hereafter). The shear measurement is based on 4.9×10^5 galaxies, and the final effective number density is 16.35 per arcmin².

The paper is organized as follows. In Section 2 we briefly introduce the shape measurements of galaxies in the VOICE survey. The image simulation procedures are detailed in Section 3. The bias calibrations of the measured shear are presented in Section 4. The bias sensitivities, especially the impact of blending effect and undetected galaxies, are discussed in Section 5. We then summarize our results in Section 6. Note that all magnitudes in this paper are quoted in the AB system (Oke & Gunn 1983).

2 WEAK LENSING SHEAR MEASUREMENTS

In this section, we summarize the procedures to measure the shear of galaxies in VOICE. More details can be found in F18.

The single exposure images after astrometric and photometric calibrations are stacked for source detection and photometry using SExtractor package (Bertin & Arnouts 1996). The stars and galaxies are then separated by combining multi-band colors and the magnitude-size relation. In total, about 150,000 galaxies and 2800 PSF stars are extracted in each tile. These PSF stars are selected to be brighter than 22.0 mag with SNR higher than 20 and have nearly uniform distribution over the entire images.

The galaxy shapes are measured for each tile individually using LensFit which is a Bayesian model fitting code. The surface brightness distributions of galaxies are modeled as a de Vaucouleurs bulge plus an exponential disk components. In LensFit,

the multiple exposures can be jointly fitted to yield the likelihoods of a given galaxy. The ellipticity is then derived by averaging the likelihoods, with a marginalization over other free parameters (i.e. the galaxy position, scalelength, flux, bulge fraction and intrinsic ellipticity) with the adopted priors (Miller et al. 2013). In the meantime, a weight is assigned to each galaxy which includes both the measurement uncertainty and the intrinsic shape of the galaxy. If a galaxy has an unsuccessful shape measurement, the corresponding weight is set to zero. Each object is also flagged with an integer to indicate its characteristics, a number of zero meaning a successful model fit to the galaxy. `LensFit` was originally developed to measure the cosmic shear in CFHTLenS (Heymans et al. 2012), and at present has also been applied to other surveys, such as KiDS (Kuijken et al. 2015; Hildebrandt et al. 2017) and RCSLenS (Hildebrandt et al. 2016).

To deblend the neighboring galaxies, `LensFit` creates isophotes after smoothing their surface brightness distributions with a Gaussian function of FWHM equal to that of the local PSF. If the isophotes of the target galaxy are touching with the neighbors at a given threshold (2σ by default) above the smoothed pixel noise, these galaxies will be excluded from further analysis. On the other hand, if the centroid of a galaxy, measured from the pixels within the threshold in the stacked stamp, does not lie within 4 pixels around the target position in the original input catalog, it is also excluded. These galaxies are either neighbors or individuals with complex morphology. With the default threshold of 2σ , we find that about one third of galaxies, similar number of galaxies compared to KiDS, have shape measurements with non-zero weight when only using the single epoch images. However, the number does not increase when more epochs are included. This can be understood as follows. The default threshold in `LensFit` is based on surveys shallower than VOICE. Increasing the depth, we have a larger number of faint detections, and therefore more rejections due to the presence of neighbors. We have performed extensive tests, and found that changing the threshold to 5σ can lead the number of galaxies with non-zero weight to a reasonable level. Therefore, we use the new threshold for shape measurement in both the observational analyses and simulation studies.

Finally, over 300,000 galaxies in the entire field have shape measurements with ellipticity dispersion of about 0.298. Following the definition in Heymans et al. (2012), the derived weighted number density is about 16.35 per arcmin² over the total effective sky coverage of 4.13 deg² after rejecting the masked regions. This is about two times larger than that of KiDS survey.

3 IMAGE SIMULATION

We use `Galsim` (Rowe et al. 2015), a widely used galaxy image simulation toolkit, to create the simulated images. `Galsim` can generate star and galaxy images with specified analytic surface brightness profiles or based on direct *HST* observations. Different image transformations and noise models can be efficiently handled by the software. A framework for simulating weak lensing shear is also encoded. In this work, the simulation is performed in two steps for each tile. As a first step, we generate a mock catalog which contains the celestial coordinates, magnitudes, morphologies and ellipticity of the simulated objects. This mock catalog is then used to create single exposure images for shape measurements.

Table 1. The fractions of neighboring galaxies in the four CDFS tiles. Galaxies are defined as neighbors if their separation is less than r .

Field	$r \leq 1.0''$	$r \leq 2.0''$	$r \leq 3.0''$
CDFS1	0.04%	4.83%	16.34%
CDFS2	0.06%	5.08%	16.73%
CDFS3	0.03%	4.42%	15.99%
CDFS4	0.05%	4.72%	16.52%

3.1 Mock Catalogs

In the simulation, we use the sources detected in the observed images as parent sample, and fix their celestial coordinates and fluxes to the observed values. This takes into account in a natural way the galaxy clustering and blending effect. Following Chang et al. (2013), we define the neighbors simply by their separation on the celestial sphere (further discussion on the definition is given in Section 5). The fraction of neighboring galaxies within a given distance r is shown in Table 1. It is seen that the fraction increases significantly as the separation gets larger, reaching about 16% for distances of $r \leq 3.0''$. These neighbors can potentially bias the shape measurements. We note that galaxies fainter than the detection limit are missing in our parent sample, but they may also introduce biases in the measured cosmic shear (Hoekstra et al. 2015, 2017; Fenech Conti et al. 2017). For the VOICE survey, however, we find that their effects are almost negligible. Detailed investigation on this systematics will be presented in Section 5. We do not include saturated stars in the parent sample. As shown in F18, they have been masked out before performing shape measurements.

As in `LensFit`, the galaxy profiles are modeled as a linear combination of a de Vaucouleurs bulge and an exponential disk components. Following Miller et al. (2013), the galaxy bulge to total flux ratio (B/T) is randomly sampled from a truncated Gaussian distribution $N(0.0, 0.1^2)$ in the range of 0.0 to 1.0, and around ten percent of galaxies are set to be bulge-dominated with $B/T = 1.0$. The intrinsic ellipticity as well as the size (defined as the disc scalelength along the major axis) distributions of the galaxies are kept the same as that in Miller et al. (2013) for CFHTLenS simulations. In the fiducial model, the dispersion of the intrinsic ellipticity is close to $\sigma_{\text{int}} = 0.25$. The relationship between the r -band magnitude and median disc scalelength involved in the size distribution follows the equation given by Kuijken et al. (2015). It should be noted that these distributions also correspond to the `LensFit` priors used for VOICE shape measurements. The orientations of the galaxies are randomly assigned, following a uniform distribution on the interval $[-\pi/2, \pi/2]$.

A constant shear with modulus $|g| = 0.04$ is applied to all galaxies. To calibrate the measured shear signal to about one per cent level, in this case, the minimum number of simulated galaxies is required to be $n_{\text{gal}} = [\sigma_{\text{int}}/(0.01|g|)]^2 \approx 3.9 \times 10^5$ (Massey et al. 2007). As shown in the following section, our simulation can satisfy the criterion. As a compromise between deriving valid shear calibration and saving computational time, four different shear combinations (g_1, g_2) are used, which are $(+0.0283, +0.0283)$, $(-0.0283, -0.0283)$, $(-0.0370, +0.0153)$, and $(+0.0153, -0.0370)$, respectively, corresponding to rotate $|g|$ by $\pi/4, 5\pi/4, 7\pi/8$, and $13\pi/8$. It is noted that by comparing the biases derived from any two or three of the combinations to that from the four combinations, the results and conclusions are identical. Though with limited number of shear combinations, we conclude that it is sufficient to yield valid bias calibrations.

3.2 Simulated Images

Based on the mock catalog above, we generate as many single exposure images as the real observations. As OmegaCam consists of 8×4 CCD chips, each one of 2047×4000 pixels with pixel scale of $0.214''$, our simulated single exposures have the same format. To mimic the dither pattern we set the pointings of the simulated images to be exactly the same as in the observation. Because the imaging was conducted in many different nights, the background noise dispersion σ_{bkg} of the observed images after sky subtraction varies, typically ranging from 10.0 ADUs to 40.0 ADUs with median of about 15.0 ADUs. Such broad distribution contributes to different noise levels for a certain galaxy between different exposures, and hence can potentially bias the shape measurement. After applying masks in the observed sky-subtracted images, we find that the distributions of the pixel noise values can be well described by a Gaussian function $N(0.0, \sigma_{\text{bkg}}^2)$. Therefore, the background noise of the simulated images is assumed to be Gaussian with σ_{bkg} fixed to that of the corresponding observation. To convert the apparent magnitudes to instrumental counts, the magnitude zeropoint is set to 24.58 mag.

For each galaxy, we note that Galsim can automatically assign a stamp size, and then project the surface brightness distribution onto the entire image stamp. The stamp size is typically larger than 30×30 pixels, corresponding to several ten times of the scale-length, even for very faint galaxies. We point out that the fluxes in the parent sample are actually measured in a given aperture which is generally smaller than the total fluxes of galaxies (Kron 1980; Bertin & Arnouts 1996). Similarly, if we again perform the same aperture photometry on the simulated images, the derived magnitudes from the stacked image will also be systematically fainter than the input, especially for those with large scalelengths, meaning that some faint galaxies in the parent sample can not be detected after adding background noise. As a result, the magnitude distributions between the simulation and observation differ, especially at the faint end. To solve the issue, we shrink the stamp size of every galaxy based on its magnitude and half-light radius. Since LensFit truncates the model surface brightness distribution at a major-axis radius of 4.5 exponential scalelengths for disc component or 4.5 half-light radii for bulge component, we fix the stamp sizes of galaxies fainter than 20.5 mag to be 12.0 half-light radii, and 15.0 half-light radii for brighter ones, moderately larger than the model truncations in LensFit. With this adjustment, over 98% of the input galaxies can be recovered in the final stacked image and the overall SNR distribution of them is consistent with observation as presented in Section 3.3.

We convolve the sheared galaxy profiles with the local PSFs, which are modeled by using the PSFEx package (Bertin 2011) through observed single-exposure images. Only stars with SNR larger than 50 are used for the PSF construction. We find that a second-order polynomial function is adequate to model the PSF variations over the entire CCD mosaic. Finally, the PSF at a given image position can be calculated by a linear combination of six pixel basis vector images. The surface brightness profiles of the PSF-smearred galaxies and stars are then rendered onto the images.

For each shear combination, two sets of images are created where the galaxies in the second set are rotated by 90 degrees before applying shear and PSF convolution in order to reduce the shape noise (Massey et al. 2007). The average of the intrinsic ellipticity is expected to be zero by this construction. In total, eight copies of each galaxy are simulated so that the total number of galaxies is about 4.8×10^6 .

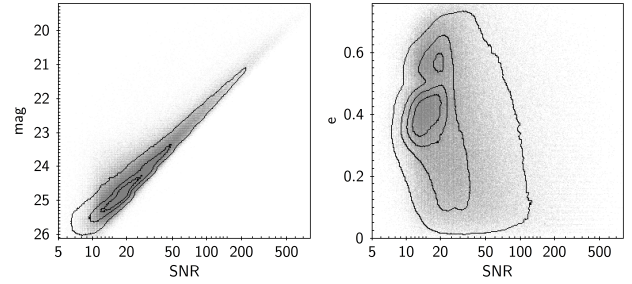


Figure 1. The two-dimensional weighted distributions of magnitudes and ellipticity versus SNR. The grayscale represents the data from VOICE observation, while the black contours are the density from simulation.

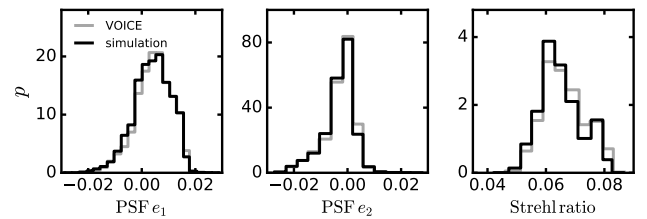


Figure 2. Comparison of the weighted distributions of PSF parameters between the simulation (black lines) and VOICE observational data (grey lines). The distributions from left to right are the two ellipticity components (e_1 and e_2) and the Strehl ratio, respectively.

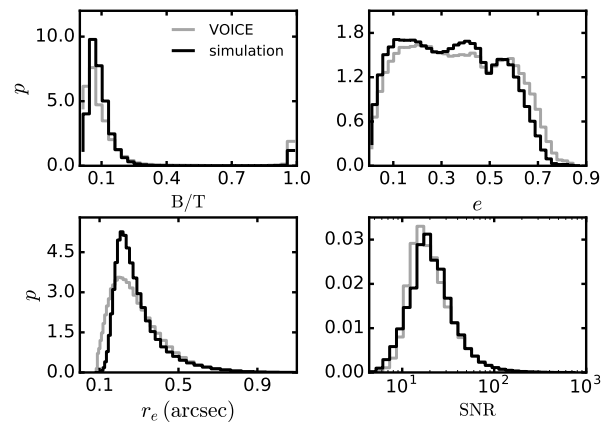


Figure 3. Comparison of the weighted distributions of galaxy parameters from the simulation (black lines) and VOICE observational data (grey lines). The distributions from left to right and top to bottom are the bulge fraction B/T, ellipticity, major-axis scalelength and SNR, respectively.

3.3 Validation of the Simulation

Though the global background noise levels of the simulated images are identical to those of observation, the local variations are not necessarily the same. As a result, the positions and magnitudes of the objects derived from the simulations do not exactly match the input values. Therefore, we stack the simulated images and re-perform source detection and photometry using SExtractor with the same parameters as in the production of the photometric catalog from the data. These new source catalogs are used for shape measurements on the simulated images.

Several cuts are then applied to the shear catalogs for bias analysis. First of all, only galaxies with non-zero weight are selected. Since the properties of galaxies are analyzed as weighted

average in the following sections, this cut does not affect our bias calibrations. We further reject the potentially problematic galaxies which are flagged as non-zero by `LensFit`. After these constraints, we match these catalogs with the mock sample using a k -d tree nearest neighbor search algorithm which is fast and efficient for large dataset. An appropriate aperture selection for the matching is essential under the existence of neighboring galaxies. A larger aperture can increase the probability of spurious matches, while too small aperture makes many faint galaxies miss out due to the noise-induced mismatch of the coordinates between simulation and observation. It is found that an aperture radius of 0.6 arcsec, corresponding to three pixels, can efficiently remove spurious detections and reduce the probability of mismatch for neighboring galaxies. Finally, about 2.3 million galaxies are obtained in the sample for bias analysis. Figure 1 shows the two-dimensional weighted distributions of magnitudes and ellipticity versus SNR for the observation and simulation data. The double-peak distribution of ellipticity is attributed to different ellipticity priors between the disc-dominated and bulge-dominated galaxies (Miller et al. 2013).

Since the dominant contribution to the shear biases results from the imperfect PSF modeling, an appropriate simulation should be capable to capture the main features of the observed PSF, especially the spatial and temporal variations. To validate the PSF model constructed by `PSFEx`, we compare the PSF parameters between the simulation and observation in Figure 2. It can be seen that the weighted distributions of the two ellipticity components and the Strehl ratio¹ parameter measured from simulated images are in good agreement with the observed data. The significant difference in distributions between the two ellipticity components implies the complicated PSF variations in the observation. One possible reason is that the long time span in observation for every tile makes the PSF pattern varied remarkably so that the distributions of the two components differ. Our PSF models, however, can properly reproduce these variations.

In addition, Figure 3 further compares the weighted distributions of some galaxy parameters measured by `LensFit` from the simulation and observed data. The bulge fraction derived from simulation is well-matched with the VOICE data. The small differences of the scalelength and SNR indicate that small and faint objects are still absent in our simulation though we have reduced the stamp size in simulation according to the galaxies' scale length and magnitude to suppress this effect. The discrepancy presumably results partly from the different intrinsic size distributions between the simulation and real observation, and the fixing of background noise dispersions in the simulation. As discussed in other studies (e.g. Miller et al. (2013)), the bias calibration primarily depends on the galaxy size r_e and SNR. Any difference in their distributions implies that the bias calibration results derived from simulation may not be applied directly to the observation. We will describe our scheme to calibrate the biases in the VOICE survey based on the simulation in the following section.

We can also see that the ellipticity distributions between the simulation and observation are different at both small and large values. Such mismatch may indicate that the intrinsic ellipticity distribution used in the simulation also differs from the real observation. Because the cosmic shear is estimated as an average of

the galaxy ellipticity, the different ellipticity distribution in the simulation probably leads to a bias which is also inappropriate to calibrate the observation (Viola et al. 2014). However, as demonstrated in the simulation of KiDS survey (Fenech Conti et al. 2017) where similar discrepancy in ellipticity distributions are presented, the resulting biases is much smaller than their expected 1.0% accuracy, and not sensitive to the variation of the intrinsic ellipticity distribution. Through changing the ellipticity distributions, similar conclusion was also drawn even in the *Euclid*-like simulation (Hoekstra et al. 2017). Therefore, we assume that the difference in the ellipticity distributions between the simulation and observation would also not significantly affect the bias calibration in this work.

4 BIAS CALIBRATION

Following Heymans et al. (2006), the accuracy of the reduced shear g_i^{obs} can be modeled in terms of the multiplicative bias m and additive bias c relating to the true shear g_i^{true} as

$$g_i^{\text{obs}} = (1 + m_i) \times g_i^{\text{true}} + c_i,$$

where g_i^{obs} denotes the weighted average of the ellipticity measured by `LensFit` and the subscript i refers to the two shear components.

The multiplicative bias and additive bias generally depend on the observed galaxy properties, such as the SNR and galaxy size. The additive bias primarily stems from the residuals in modeling the PSF anisotropy. It can be empirically corrected using the observed data. The multiplicative bias, a change of the amplitude of the shear, is mainly attributed to the background noise and pixelation, and most likely affects the shape estimate of faint galaxies. It is generally calibrated through image simulations.

In this section, we perform detailed bias calibrations for the measured galaxy shape. We note that the binning strategy for each observable adopted in this work is by equalizing the total number of galaxies in each bin. The weighted average is assigned as the center of each bin for the corresponding observable. We use the bootstrap method with 100 realizations to derive the uncertainties of the estimated shear in each bin. The χ^2 minimization is then applied to yield the multiplicative and additive biases as well as the associated uncertainties.

4.1 Selection Bias

Besides the bias resulting from noise and model fitting, the source detection and shape measurement procedures can also introduce bias. This kind of bias is usually referred as selection bias and it was extensively discussed in many studies through image simulations (Kaiser 2000; Bernstein & Jarvis 2002; Hirata & Seljak 2003; Heymans et al. 2006). Due to the difficulties in accurately measuring the shape of faint and small galaxies for many shape measurement methods, these galaxies suffer from more severe selection bias than the bright ones. Therefore, the bias is expected to be a function of the magnitude (or equivalently the SNR) and galaxy size, and can arise in both the observation and simulation. In the KiDS simulation, Fenech Conti et al. (2017) reported a significant multiplicative selection bias which was as large as 4.4% after averaging the true sheared ellipticity of galaxies with non-zero weights. It showed an obvious dependence on the magnitude and major-axis scalelength r_e . However, the dependency is reduced when we consider the geometric average of the major- and minor-axis scalelengths, denoted

¹ The Strehl ratio is generally defined as the ratio of the peak aberrated intensity relative to the maximum attainable intensity from a point source in diffraction-limited optical system. In `LensFit`, it is defined as the fraction of PSF light contained in the central pixel.

as r_{ab} , because it is less correlated with the measured ellipticity affected under the existence of pixel noise.

In our simulation, we quantify the selection bias by analyzing the input sheared ellipticity of galaxies in terms of the observables by following a similar scheme. As described in Section 3, only galaxies detected in the observations are used to generate the simulated images, and we find similar number of galaxies with shape measurements compared to that of observation. For those galaxies detected in the simulated mosaic images using SExtractor, the selection bias is derived by comparing the average of the input true sheared ellipticity with true shear. In this case, the effect of noise bias vanishes, and biases stemming from the detection procedures, including the potential cancellation of zero shape noise implementation due to undetected galaxies, are dominant. It turns out that the selection bias is almost negligible at this stage. We find, however, that the multiplicative selection bias increases to 0.025 for the two shear components for galaxies only with non-zero weight after running LensFit. The top panel of Figure 4 displays the dependence of the selection bias on magnitude. It can be seen that the multiplicative selection bias presents nearly stable trend around zero at magnitude brighter than 24.0 mag, while it increases dramatically at fainter magnitudes because the effect of noise on the shape measurement becomes significant for faint galaxies. Similar trend can also be seen for the additive bias. The multiplicative bias also exhibits a strong dependence on the major-axis scalelength r_e , as shown in the bottom panel of Figure 4. However, an apparent lower correlation is derived by adopting r_{ab} , although the additive bias does not present significant correlation with either definition of the galaxy size. As a result, instead of r_e , we use r_{ab} as the proxy of galaxy size in this work to perform bias calibration.

As discussed above, the shear signal measured from both simulation and observation is supposed to be subjected to the selection bias. Therefore, to calibrate the shear in the VOICE survey, it is essential to take into account all the sources of bias, including the selection bias, the noise and model biases, through our simulation. In the following sections, we systematically investigate the bias calibration based on the observables SNR and r_{ab} since they are the two predominant quantities that the bias depends on.

4.2 Empirical Calibration

The biases of the shear measured from the simulation as a function of galaxy SNR and size are shown in Figure 5. As expected, both the multiplicative bias and additive bias get larger for galaxies with low SNR and small size. The maximum of the absolute values reaches 0.4 for multiplicative bias and 0.008 for additive bias. On the other hand, as the increase of both SNR and size, the multiplicative bias becomes stable but negative which implies the complicated dependence between the systematics and observables presented in the observation. Furthermore, one striking feature shown in Figure 5 is that the two components for both multiplicative and additive biases present different amplitudes. It may again be attributed to the long-time observing period for each tile. Unlike other weak lensing observations that usually complete one tile (or one pointing) in one night with sequential exposures, the observational strategy for VOICE could result in considerably different patterns of the PSF distributions (see Figure 2) and thus make the two bias components different. Therefore, a simple analytical approximation, such as the function adopted in Miller et al. (2013), is apparently not adequate to fit the data. Instead, similar to the strategies proposed in KiDS simulation (Fenech Conti et al. 2017) we use the bin-matching method on the SNR– r_{ab} surface to cali-

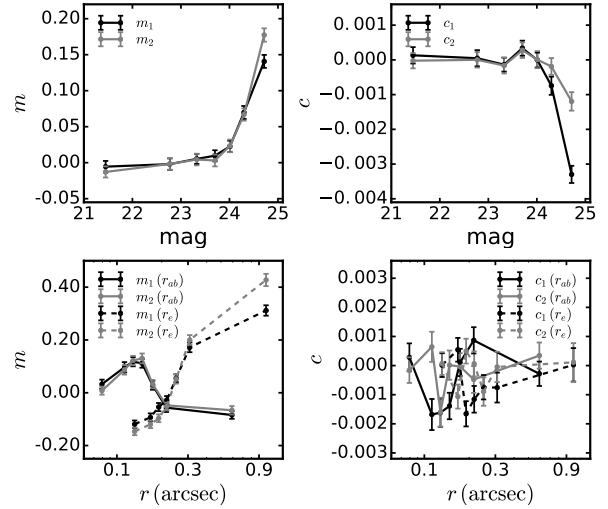


Figure 4. *Top panel:* the multiplicative and additive selection biases as a function of magnitude for galaxies with non-zero weight. *Bottom panel:* the multiplicative and additive selection biases as a function of galaxy size. The solid lines represent the size r_{ab} defined as the geometric average of the major- and minor-axis scalelengths, while the dashed lines indicate the scalelength r_e along major axis. Note that both of them are calculated through LensFit output.

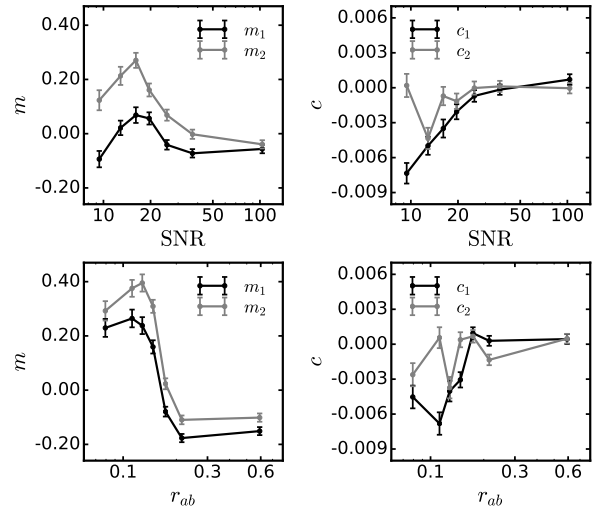


Figure 5. The multiplicative and additive biases of the measured shapes as a function of SNR (*top panel*) and size (*bottom panel*).

brate the bias. Specifically, we firstly bin the galaxies by SNR and size r_{ab} in the two-dimensional plane, and then derive a constant bias in each bin. If one observed galaxy falls into a certain bin its ellipticity will be calibrated by applying the corresponding biases.

Due to our limited sky coverage and relatively small amount of galaxies, an appropriate binning scheme is crucial to derive valid bias calibration results by using this method. If the number of bins is too small, we may miss out on some real features in the bias surface. However, the statistical uncertainty arises if there are too many bins, and that can result in extra artificial bias. For our simulation, we find that a five-bin scheme along both SNR and r_{ab} axis can yield robust calibration. In this case, the average error of the multiplicative bias in each bin is 0.04, while the SNR_m (defined as m/m_{err} , where m_{err} is the estimated error of m) is close to 4.8. The

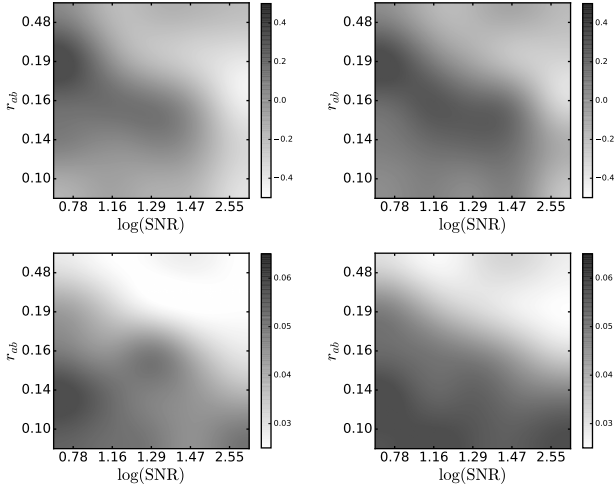


Figure 6. *Top panel:* Multiplicative bias distributions (m_1 on the left and m_2 on the right) in the $\text{SNR} - r_{ab}$ two-dimensional plane. For clarity, a “lanczos” kernel is applied to smooth the discrete values. *Bottom panel:* Estimated error distributions of the multiplicative biases.

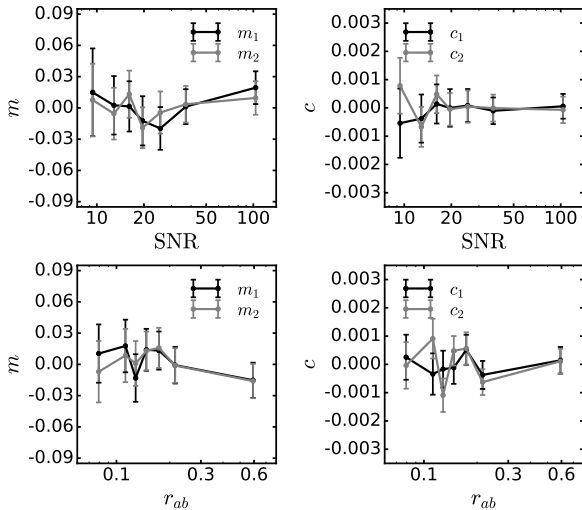


Figure 7. The residual multiplicative and additive biases after calibration using the bin-matching method as a function of measured SNR (*top panel*) and size (*bottom panel*).

top panel of Figure 6 illustrates the two-dimensional distributions of the two multiplicative bias components in the $\text{SNR} - r_{ab}$ plane. It is also seen that though they present similar dependence on the two observables, the amplitudes of m_2 are systematically larger. The distributions of corresponding error m_{err} are shown in the bottom panel. As expected, galaxies with smaller size and lower SNR suffer more significant calibration uncertainties. Figure 7 shows the final residuals after bias calibration. It can be seen that the multiplicative bias is well within 0.03 over the entire SNR and size ranges, and the additive bias almost vanishes. The residuals do not present strong dependence on the SNR and galaxy size. For the entire simulation data without binning, both the residual multiplicative bias and additive bias are consistent with zero, indicating that the calibration is unbiased.

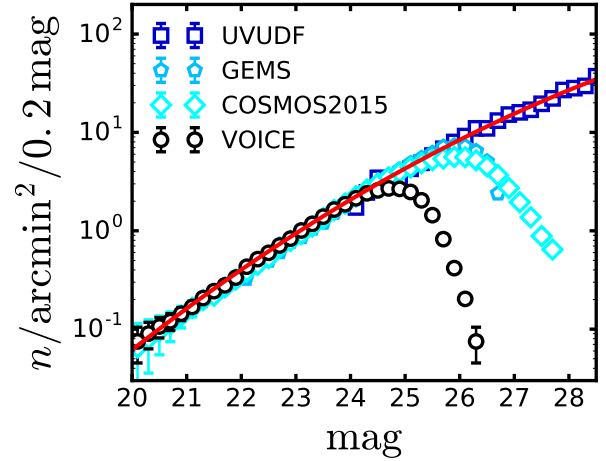


Figure 8. Magnitude distributions of different r -band photometric catalogs with errorbar estimated by the Poisson statistics. The magnitudes are from UVUDF F606W band (blue), GEMS F606W band (light blue), COSMOS2015 r band (cyan) and VOICE r band (black), respectively. The red solid line represents the best fit for VOICE $20.0 < m_r < 24.0$, GEMS $24.0 < m_r < 26.0$ and UVUDF $26.0 < m_r < 28.0$ data.

5 CALIBRATION SENSITIVITY

As we have discussed in Section 3, the sample extracted from simulation lacks faint and small size galaxies. The distributions of the ellipticity between the simulation and observation are also slightly different. These differences may result in extra residual bias when applying the calibration results to observation. Hoekstra et al. (2017) studied the sensitivities based on *Euclid*-like image simulation, and concluded that the multiplicative bias is indeed affected by these factors. However, they demonstrated that the amplitude change of the multiplicative bias is always less than 0.005 by varying the corresponding distributions. Similar conclusions were also drawn in the KiDS simulation (Fenech Conti et al. 2017), which stated that the sensitivities of the multiplicative bias to the different distributions can be safely neglected for the present accuracy requirement ($m \sim 0.01$) in weak lensing surveys. VOICE and KiDS surveys share the same instrument and observational configuration. The VOICE survey is deeper, but the area is much smaller than that of KiDS. Thus the number of galaxies with successful shear measurements is smaller, resulting in larger statistical uncertainties in cosmological analyses. We therefore expect that the effect of lacking of small and faint galaxies in our simulation on the shear bias calibration is even less significant than that of KiDS. However, for future deep and wide surveys, this can be an issue (Hoekstra et al. 2017).

On the other hand, since the galaxies in our simulation are only from observation without including those below detection limit, the undetected galaxies may introduce potential bias. In addition, since the positions of galaxies in the simulated images exactly match those of real galaxies, it is possible to study the impact of the galaxy blending effect on the multiplicative bias. We focus on the sensitivity analyses of the two factors in this section.

5.1 Impact of Galaxies Below Detection Limit

For objects fainter than the limiting depth, Hoekstra et al. (2015) found that they make the multiplicative bias of brighter galaxies underestimated in cluster environment because they are likely to

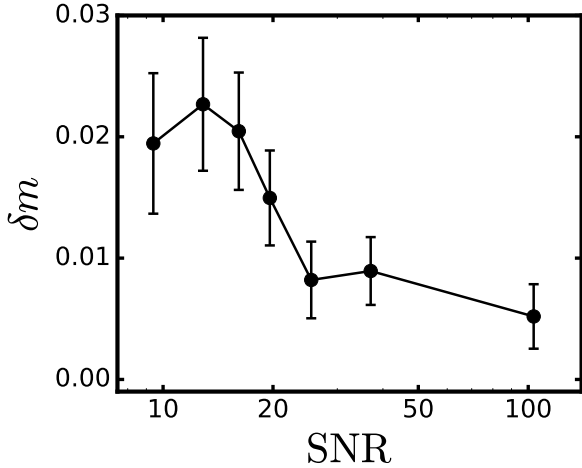


Figure 9. Residual multiplicative bias δm due to the presence of undetected galaxies as a function of SNR.

be blenders or skew the background noise. [Hoekstra et al. \(2017\)](#) further analyzed the issue, and found that the multiplicative bias is affected by both the size distribution and count slope of the undetected galaxies. [Fenech Conti et al. \(2017\)](#) also discussed the effect of these undetected objects in KiDS simulation and found negligible change in bias compared to the survey accuracy.

To mimic the realistic magnitude distribution of the undetected galaxies in VOICE observation, photometric measurements from other deeper imaging are included, which are *HST*/ACS *F606W*-band data from UVUDF ([Rafelski et al. 2015](#)) and GEMS ([Rix et al. 2004](#); [Griffith et al. 2012](#)), Subaru/SuprimeCam *r*-band data from COSMOS2015 catalog ([Laigle et al. 2016](#)). These filters are analogous to the OmegaCam *r* filter. Figure 8 shows their number density distributions of galaxies as a function of magnitude m . A second order polynomial is adopted to fit the distribution using VOICE counts between $20.0 < m_r < 24.0$, GEMS counts between $24.0 < m_r < 26.0$ and UVUDF counts between $26.0 < m_r < 28.0$. The least-square result is

$$\log(n) = -15.012 + 0.947m_r - 0.013m_r^2,$$

where n is the number of galaxies per square arcminute in a given magnitude bin with width of 0.2 mag. In our simulation, we truncate the magnitude of undetected galaxies to 28.0 mag, and restrict their bright-end to 25.0 mag which is approximately equal to the maximal value in the distribution of VOICE catalog, as depicted in Figure 8. Consequently, the total number density of these undetected galaxies is as many as 185 per square arcminute.

Unlike the simulation of the detected galaxies as described in Section 3, the celestial positions of the undetected galaxies are randomly assigned. The size and intrinsic ellipticity are drawn from the same prior distributions as stated in [Miller et al. \(2013\)](#). Since these galaxies are below the noise level even in the stacked image, extra shear components are not expected to contribute significant systematics. Therefore, null shear is assigned to these galaxies. Furthermore, to save simulation time, we do not generate the undetected galaxy images chip by chip as for the procedure for the detectable ones. Instead, we sprinkle them to a noiseless image mosaic centered at the same celestial position as that of the CDFS field. The PSF model is assumed to be Gaussian with constant FWHM fixed to the median value of the observation. Finally, for a given CCD chip (or sky coverage), we extract the corresponding sub-

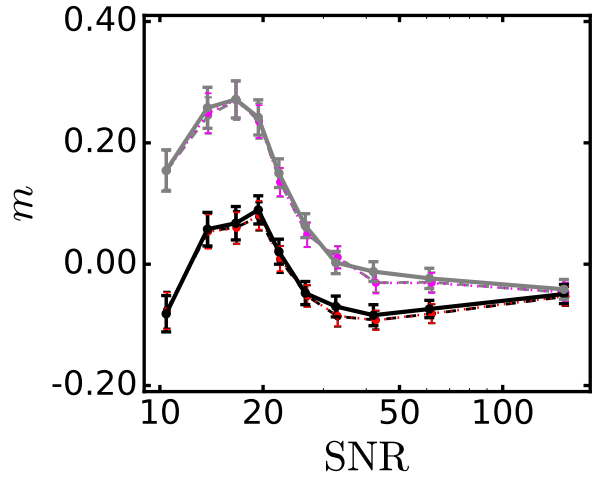


Figure 10. The multiplicative bias as a function of SNR. The black and grey dashed lines represent the two bias components m_1 and m_2 derived from the entire simulation sample, while the solid lines are the corresponding components after rejecting the neighboring galaxies. The dotted lines indicate the average bias derived from the subsamples of galaxies by repeated sampling 100 times.

Table 2. The ellipticity dispersions of the neighboring galaxies in the four fields. Column 1 represents the maximum distance between any galaxy pair. The number of galaxies with non-zero weight and zero flag is shown in Column 2, while Column 3 indicates the fraction relative to the neighboring galaxies without any cut. Column 4&5 are the dispersions of the two ellipticity components.

r	n_{gal}	fracion	σ_{e_1}	σ_{e_2}
1.0''	124	33.6%	0.403	0.421
2.0''	1858	7.8%	0.333	0.350
3.0''	25746	31.6%	0.307	0.309

image from this image mosaic, and then add it to the previously simulated image.

We follow the same steps as presented in previous sections to perform shear measurements and bias analyses for the detected galaxies using the new set of images. Compared to the results derived from no-faint-galaxies simulation, the multiplicative bias of the entire sample increases only by 0.003, while the additive bias shows negligible change. Figure 9 shows the residual multiplicative bias δm as a function of SNR. Here δm is defined as $[(\delta m_1)^2 + (\delta m_2)^2]^{1/2}$, where δm_i represents the difference of multiplicative biases between the two sets of simulation. Overall, our result indicates that galaxies with lower SNR (or fainter magnitude) suffers from more significant impact due to the undetected galaxies. Since the amplitude is well below the residual bias we achieve in Section 4, we claim that the sensitivity of the multiplicative bias to the undetected galaxies for our simulation is insignificant. However, as illustrated in Figure 9 the impact of undetected galaxies has to be taken into account for more accurate shear measurements as required by future large and deep surveys, especially for galaxies with low SNRs.

5.2 Impact of Blending Galaxies

As discussed above, the simulation strategy in this work enables us to study the effect of the neighboring galaxies on the measured shear. These galaxies can be either physically related neighbors

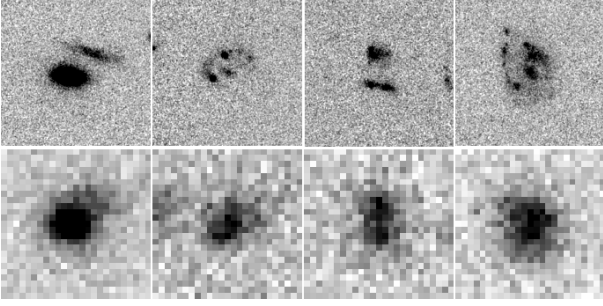


Figure 11. Examples of four very close neighbors in CDFS1/GEMS field. The top panel shows galaxies observed in GEMS survey, while the corresponding stacked images from the VOICE survey are displayed in bottom panel. The size of each stamp is $5'' \times 5''$, centered on the target galaxy in VOICE image.

which have similar shear or projected close pairs but with different redshifts and shape distortions. Though `LensFit` has encoded an algorithm to deal with them (Miller et al. 2013), potential bias is still inevitable in the measured shear due to the inappropriate modeling of the surface brightness distributions in the overlapped regions. In this part, we mainly concentrate on their contribution to the multiplicative bias.

First of all, we compare the ellipticity dispersions of the real galaxies in the parent samples. As shown in Table 2, the dispersion increases as the neighbors get closer to each other, and is always larger than that of all galaxies in the full sample. We note that a large fraction of the neighbors with separation less than $1.0''$ have non-zero weight. Since most of them are pairs, careful analysis indicates that almost all of the pairs show very similar ellipticity components and other properties, meaning that they are identified as single and extended galaxies by `LensFit` but with slightly different position marginalization. As a result, the ellipticity dispersion is almost 38.0% larger than the average level. These galaxies should be excluded from further shear analyses. It can also be seen that about 31.6% of the neighboring galaxies within separation $r = 3.0''$ have shape measurements (or equivalently about 8.23% of non-zero weighted galaxies in the observation sample are neighbors), though most have been excluded by `LensFit`. The ellipticity dispersion of these remainders still exhibits 3.4% larger than the average value. The weighted number density of them is about 1.28 per square arcmin. Therefore, simply rejecting these neighbors can result in a considerable decrease in the weighted number density. However, by comparing the shear two-point correlation functions between the full sample and that after rejecting $r \leq 3.0''$ neighbors we find that they show almost identical results, which indicates that the impact of neighbors on our statistical analyses of the measured shear is negligible, given the relatively large statistical uncertainties of the VOICE shear sample.

We further quantify their impact on the multiplicative bias. In that case, a simple distance cut to separate the neighbors from the full sample is not sufficient because many neighbors selected by this method have very small sizes (or relatively large flux concentrations) so that their overlapped surface brightness distributions do not significantly affect their shape measurements. This kind of neighbors can dilute the impact of blending effect on the multiplicative bias. Therefore, to emphasize the effect, we redefine the neighbors as galaxies with separation smaller than four times of the sum of their major-axis scalelengths. Under this definition, the fraction of neighbors with shape measurements reduces to about 6%. A clean simulation sample is then constructed by rejecting these

neighbors. The solid lines in Figure 10 show the two multiplicative bias components, derived from the clean sample, as a function of SNR. For comparison, the bias components from the full sample are illustrated as dashed lines. As it can be seen, the biases are consistent at $\text{SNR} < 20.0$, while the amplitudes of the two bias components become systematically smaller for the clean sample. This may indicate that the SNRs of the neighbors are systematically overestimated by `LensFit` so that they mainly affect the bias calibration at high SNR. It turns out that the median of the SNRs for the neighboring galaxies is 33.0, indeed larger than the value of 24.2 for the full sample. However, the change of the bias for the clean sample may be also attributed to the decrease of galaxy count. To check the possibility, we randomly select an equal number of galaxies as the clean sample from the full simulation sample, and estimate the multiplicative bias. The sampling procedure is repeated by one hundred times. The dotted lines in Figure 10 show the average of the bias as a function of SNR. Both the bias components present good agreement with the full sample, indicating that the neighbors do contribute extra multiplicative bias, especially at high SNR. The weighted average bias resulting from the blending effect is about 0.002 by comparing the clean sample to the full simulation sample.

Besides the neighbors that can be unambiguously identified, some are so close that they are detected as single objects by `SExtractor` or other source detection methods. Since the seeing of ground-based imaging is typically comparable or larger than the separation between such blenders, we are not able to distinguish them from those real isolated objects. The only feasible way to separate them is through comparing their images to the observation with higher image resolution or better seeing condition, such as space-based observations. The modest overlapping region ($\sim 800 \text{ arcmin}^2$) between the VOICE survey and the Galaxy Evolution From Morphology And SEDs (GEMS; Rix et al. (2004)) survey enables us to quantitatively study the properties of these close blenders. We identified 2185 blenders down to magnitude of 26.0 mag in our sample by following the similar method in Dawson et al. (2016), accounting about 5.0% relative to the total number of galaxies in the same field. We find that 68% of them have shape measurements with dispersion of 0.33 for the two ellipticity components. Their weighted number density is 0.92 per arcmin^2 . Figure 11 exhibits four typical examples of these blenders. Apparently, they are observed as multiple objects in the GEMS survey, and show diverse morphologies, though they can only be detected as single galaxies in the VOICE survey. It is not expected that the measured shape is correct so that it can potentially bias the final shear calibration for the entire sample. For the current weak lensing surveys, however, the small fraction of such blenders is not expected to affect the accuracy of the cosmic shear too much. For upcoming deep and wide surveys, especially the ground-based surveys, we do need to quantify the effect of them on the measured shear, and subsequently on cosmological studies.

6 SUMMARY

The VOICE survey has observed $\sim 4 \text{ deg}^2$ in the CDFS field in *ugri* optical bands using VST/OmegaCam. After a cut in $\text{FWHM} < 0.9 \text{ arcsec}$, the survey consists of more than a hundred exposures for each tile, and the depth is about 1.2 magnitude deeper than KiDS survey. We have performed shear measurements, and obtained an effective number density of galaxies $n_g \sim 16.35 \text{ arcmin}^{-2}$ (Fu et al. 2018, in preparation). In the work, we perform detailed shear bias calibrations in the VOICE survey based on *r*-band image sim-

ulation. Many observational conditions, such as the dithering pattern, background noise, celestial positions and brightness of the detected objects, have been considered in the simulations in order to mimic the real observation. The PSFEx package is used to model the spatial variations of the PSF in every exposure. The simulated single exposure images are generated by the Galsim toolkit, and the galaxy shapes are measured by LensFit, a Bayesian fitting code that has been extensively applied to many other large surveys, such as CFHTLenS, KiDS and RCSLenS. Overall, our simulation presents good agreements with the observation, especially the distributions of the PSF parameters. We notice that some small and faint galaxies are missing in our simulations comparing to the real observations. We argue that they should not affect our shear calibration significantly given the relatively low total number of galaxies in the VOICE survey. We apply the bin-matching method to the SNR and size surface to calibrate the bias of the simulation data. The final residual multiplicative bias can reach to an accuracy of 0.03 with negligible additive bias in different SNR and size bins. The average bias of the full sample is consistent with zero.

Our studies demonstrate the applicability of Lensfit for shear measurements to data with more than a hundred exposures. The image simulation analyses show that the change of the deblending threshold from the fiducial 2σ to 5σ does not introduce considerable issues.

We further discuss the sensitivity of the bias calibration to the undetected and neighboring objects. The undetected objects are likely to skew the background noise so that they can potentially bias the shape measurements of galaxies, especially those with low SNR. Taking the depth and noise level, and the relatively large statistical uncertainties into account, we find that the impact of the undetected galaxies is negligible for the VOICE survey. Additionally, we highlight the bias resulting from galaxy blending effect. Though a large fraction of neighboring galaxies has been excluded by LensFit, there are still 31.6% of neighboring galaxies with shape measurements. The ellipticity dispersion of them is 3.4% larger than the average value, and the weighted number density is as large as 1.28 per square arcmin. These neighbors contribute to 0.2% multiplicative bias compared to the full simulation sample. With the increase of depth and sensitivity, many weak lensing surveys, such as HSC and LSST, aiming to achieve more accurate cosmic shear measurements, have to deal with the blending effect more carefully.

ACKNOWLEDGEMENTS

We thank Jun Zhang for helpful comments on the image simulation. The research is supported in part by NSFC of China under the grants 11333001, 11173001 and 11653001. L.P.F. acknowledges the support from NSFC grant 11673018, 11722326 & 11333001, STCSM grant 16ZR1424800 and SHNU grant DY1201603. X.K.L. acknowledges the support from YNU Grant KC1710708 and General Financial Grant from China Postdoctoral Science Foundation with Grant No. 2016M591006. M.V. acknowledges support from the European Commission Research Executive Agency (FP7-SPACE-2013-1 GA 607254), the South African Department of Science and Technology (DST/CON 0134/2014) and the Italian Ministry for Foreign Affairs and International Cooperation (PGR GA ZA14GR02). M.P. acknowledges support from ASI-INAF grant 2017-14-H.O: Studies for the High Energy Community: Data Analysis, Theory and Simulations. Support for G.P. is provided by the Ministry of Economy, Development, and Tourism's

Millennium Science Initiative through grant IC120009, awarded to The Millennium Institute of Astrophysics, MAS

Based on data products from observations made with ESO Telescopes at the Paranal Observatory under ESO programme ID 179.A-2005 and on data products produced by TERAPIX and the Cambridge Astronomy Survey Unit on behalf of the UltraVISTA consortium.

Some/all of the data presented in this paper were obtained from the Mikulski Archive for Space Telescopes (MAST). STScI is operated by the Association of Universities for Research in Astronomy, Inc., under NASA contract NAS5-26555. Support for MAST for non-HST data is provided by the NASA Office of Space Science via grant NNX09AF08G and by other grants and contracts.

REFERENCES

- Abbott, T., Abdalla, F. B., Allam, S., et al. 2016, *Phys. Rev. D*, 94, 022001
- Bartelmann, M., & Maturi, M. 2017, *Scholarpedia*, 12, 32440
- Becker, M. R., Troxel, M. A., MacCrann, N., et al. 2016, *Phys. Rev. D*, 94, 022002
- Benjamin, J., Heymans, C., Semboloni, E., et al. 2007, *MNRAS*, 381, 702
- Bernstein, G. M., & Jarvis, M. 2002, *AJ*, 123, 583
- Bertin, E., & Arnouts, S. 1996, *A&AS*, 117, 393
- Bertin, E. 2011, *Astronomical Data Analysis Software and Systems XX*, 442, 435
- Bosch, J., Armstrong, R., Bickerton, S., et al. 2017, arXiv:1705.06766
- Botticella, M. T., Cappellaro, E., Greggio, L., et al. 2017, *A&A*, 598, A50
- Bridle, S., Shawe-Taylor, J., Amara, A., et al. 2009, *Annals of Applied Statistics*, 3, 6
- Cappellaro, E., Botticella, M. T., Pignata, G., et al. 2015, *A&A*, 584, A62
- Chang, C., Jarvis, M., Jain, B., et al. 2013, *MNRAS*, 434, 2121
- Dawson, W. A., Schneider, M. D., Tyson, J. A., & Jee, M. J. 2016, *ApJ*, 816, 11
- de Jong, J. T. A., Verdoes Kleijn, G. A., Boxhoorn, D. R., et al. 2015, *A&A*, 582, A62
- Falocco, S., Paolillo, M., Covone, G., et al. 2015, *A&A*, 579, A115
- Fenech Conti, I., Herbonnet, R., Hoekstra, H., et al. 2017, *MNRAS*, 467, 1627
- Fu, L.-P., & Fan, Z.-H. 2014, *Research in Astronomy and Astrophysics*, 14, 1061-1120
- Giacconi, R., Rosati, P., Tozzi, P., et al. 2001, *ApJ*, 551, 624
- Grado, A., Capaccioli, M., Limatola, L., & Getman, F. 2012, *Memorie della Societa Astronomica Italiana Supplementi*, 19, 362
- Green, J., Schechter, P., Baltay, C., et al. 2012, arXiv:1208.4012
- Griffith, R. L., Cooper, M. C., Newman, J. A., et al. 2012, *ApJS*, 200, 9
- Heymans, C., Van Waerbeke, L., Bacon, D., et al. 2006, *MNRAS*, 368, 1323
- Heymans, C., Van Waerbeke, L., Miller, L., et al. 2012, *MNRAS*, 427, 146
- Heymans, C., Groucutt, E., Heavens, A., et al. 2013, *MNRAS*, 432, 2433
- Hildebrandt, H., Choi, A., Heymans, C., et al. 2016, *MNRAS*, 463, 635
- Hildebrandt, H., Viola, M., Heymans, C., et al. 2017, *MNRAS*, 465, 1454
- Hirata, C., & Seljak, U. 2003, *MNRAS*, 343, 459
- Hoekstra, H., Herbonnet, R., Muzzin, A., et al. 2015, *MNRAS*, 449, 685
- Hoekstra, H., Viola, M., & Herbonnet, R. 2017, *MNRAS*, 468, 3295
- Jarvis, M., Sheldon, E., Zuntz, J., et al. 2016, *MNRAS*, 460, 2245
- Kaiser, N. 2000, *ApJ*, 537, 555
- Kilbinger, M., Fu, L., Heymans, C., et al. 2013, *MNRAS*, 430, 2200
- Kilbinger, M. 2015, *Reports on Progress in Physics*, 78, 086901
- Kitching, T. D., Miller, L., Heymans, C. E., van Waerbeke, L., & Heavens, A. F. 2008, *MNRAS*, 390, 149
- Kitching, T. D., Balan, S. T., Bridle, S., et al. 2012, *MNRAS*, 423, 3163
- Kron, R. G. 1980, *ApJS*, 43, 305
- Kuijken, K., Heymans, C., Hildebrandt, H., et al. 2015, *MNRAS*, 454, 3500
- Laigle, C., McCracken, H. J., Ilbert, O., et al. 2016, *ApJS*, 224, 24
- Laureijs, R., Amiaux, J., Arduini, S., et al. 2011, arXiv:1110.3193
- Liu, X., Li, B., Zhao, G.-B., et al. 2016, *Physical Review Letters*, 117, 051101

- LSST Science Collaboration, Abell, P. A., Allison, J., et al. 2009, arXiv:0912.0201
- Mandelbaum, R., Rowe, B., Bosch, J., et al. 2014, ApJS, 212, 5
- Mandelbaum, R., Rowe, B., Armstrong, R., et al. 2015, MNRAS, 450, 2963
- Mandelbaum, R. 2017a, arXiv:1710.03235
- Mandelbaum, R., Lanusse, F., Leauthaud, A., et al. 2017b, arXiv:1710.00885
- Massey, R., Heymans, C., Bergé, J., et al. 2007, MNRAS, 376, 13
- Miller, L., Kitching, T. D., Heymans, C., Heavens, A. F., & van Waerbeke, L. 2007, MNRAS, 382, 315
- Miller, L., Heymans, C., Kitching, T. D., et al. 2013, MNRAS, 429, 2858
- Miyazaki, S., Komiyama, Y., Nakaya, H., et al. 2012, Proc. SPIE, 8446, 84460Z
- Oke, J. B., & Gunn, J. E. 1983, ApJ, 266, 713
- Oliver, S., Rowan-Robinson, M., Alexander, D. M., et al. 2000, MNRAS, 316, 749
- Rafelski, M., Teplitz, H. I., Gardner, J. P., et al. 2015, AJ, 150, 31
- Rix, H.-W., Barden, M., Beckwith, S. V. W., et al. 2004, ApJS, 152, 163
- Rowan-Robinson, M., Lari, C., Perez-Fournon, I., et al. 2004, MNRAS, 351, 1290
- Rowe, B. T. P., Jarvis, M., Mandelbaum, R., et al. 2015, Astronomy and Computing, 10, 121
- Samuroff, S., Bridle, S. L., Zuntz, J., et al. 2017, arXiv:1708.01534
- Tozzi, P., Rosati, P., Nonino, M., et al. 2001, ApJ, 562, 42
- Vaccari 2015, Proceedings of "The many facets of extragalactic radio surveys: towards new scientific challenges" Conference, 20-23 October 2015, Bologna, Italy, Proceedings of Science, 267, 27
- Vaccari 2016a, Proceedings of "The Universe of Digital Sky Surveys" Conference, 25-28 November 2014, Naples, Italy, Astrophysics and Space Science Proceedings, 42, 71
- Vaccari et al. 2016b, Proceedings of the 4th Annual Conference on High Energy Astrophysics in Southern Africa, 25-26 August 2016, Cape Town, South Africa, Proceedings of Science, 275, 26
- Viola, M., Kitching, T. D., & Joachimi, B. 2014, MNRAS, 439, 1909